Measurement and Analysis of Neutron Energy Spectra from Fission Sources

Los Alamos
NATIONAL LABORATORY

Los Alamos National Laboratory is operated by the University of California for the United States Department of Energy under contract W-7405-ENG-36.

Edited by Anne Garnett, Group IS-1
Photocomposition by Charles Calef, Group IS-1

This work was supported by the US Department of Energy, Office of Research and Development of the Office of Intelligence and National Security.

An Affirmative Action/Equal Opportunity Employer

LA-12627-MS

UC-700
Issued: November 1993

Measurement and Analysis of Neutron Energy Spectra from Fission Sources

Roger C. Byrd
George F. Auchampaugh
William C. Feldman

Los Alamos
NATIONAL LABORATORY
Los Alamos, New Mexico 87545

MEASUREMENT AND ANALYSIS OF NEUTRON ENERGY SPECTRA FROM FISSION SOURCES

by

Roger C. Byrd, George F. Auchampaugh, and William C. Feldman

ABSTRACT

Measurements of neutron energy spectra are usually much more difficult than spectral measurements for other types of radiation. Because neutrons are uncharged, they can be detected only by nuclear interactions, either neutron capture or neutron scattering, neither of which provides an efficient method for spectroscopy at fission energies. A new scintillator technology combines the scattering and capture approaches to provide an electronically "black" detector, one that registers energy deposition only for neutrons that are totally absorbed. Using a prototype of such an instrument, we obtained spectral measurements for several fission sources at distances up to 11 m. Examples from these measurements serve to explain the detection principle, the instrument calibration, and the techniques for data analysis. A companion paper describes techniques for obtaining directional measurements, and subsequent papers will focus on particular features of the individual spectra and discuss comparisons with calculations.

---

1. INTRODUCTION

Radioactive Emissions from Nuclear Materials. One of the clearest signatures for locating and identifying nuclear warheads or the radioactive material they contain is the penetrating radiation they emit—neutrons, gamma rays, and x-rays. Each of these neutral radiations has characteristics that provide particular advantages and disadvantages for detection purposes. Of the two electromagnetic radiations, x-rays have low penetration and can be easily shielded by small amounts of dense materials such as lead. Gamma rays are very penetrating, but they are often regarded as too intrusive because of the potentially detailed spectroscopic and structural information they can provide. As a result, neutrons have often emerged as the consensus for detection, because the nature of their production and interaction sets intrinsic limits on the amount of information available. For neutron sources, the emission and attenuation mechanisms are generally nonspecific as to materials and geometries; for neutron detectors, the limited position and energy resolution assures the protection of design information. In practice, simple neutron counters are often used in combination with more intrusive gamma-ray instruments; the low natural background

of neutrons makes any signal potentially suspicious, and conclusive identification can then be made using gamma-ray spectroscopy.

Conventional Neutron Spectroscopy. Extending the options for nuclear search and identification by including measurements of neutron energy spectra would improve background rejection and provide additional information about source characteristics. Traditional neutron spectrometers have been based on three different techniques, each requiring some spectral unfolding. At low energies (below 2 MeV), proportional chambers filled with ^{3}He gas use the exothermic ^{3}He(n,p)T capture reaction, whose recoiling p and T ions provide an energy-loss peak that improves the unfolding reliability.[1] At somewhat higher energies, neutron scattering in high-pressure ^{3,4}He gas scintillators also provides relatively simple recoil spectra.[2] Unfortunately, the low efficiency of these gas-detector techniques limits their usefulness for fission sources, whose yield decreases rapidly at higher energies. As a result, the traditional method of making spectral measurements for neutron fluxes in the 1–10 MeV range uses neutron scattering in an organic scintillator. In this case, the response of standard scintillators to gamma-ray backgrounds requires that neutron measurements be made using special liquid scintillators, which produce light pulses with different decay times for recoil protons (from scattered neutrons) and electrons (from gamma-ray scattering or absorption). Unfortunately, these "pulse-shape discrimination" (PSD) techniques become problematic as the neutron energy decreases to near 1–2 MeV.[3] Thus, although PSD and spectral unfolding have long been employed in laboratory situations, no portable instrument is commercially available, and the technique is rarely used in field applications. For nuclear weapons, examples of spectral measurements and companion calculations have been published in several classified Los Alamos National Laboratory (LANL) reports as part of a Department of Energy (DOE) study of the intrinsic radiation dosages from nuclear weapons (INRAD).

Boron-Loaded Scintillators. To provide an alternative for applications in space physics, LANL worked with Bicron Corporation* to develop a new type of fast-neutron spectrometer. The technique uses a special boron-loaded plastic scintillator marketed under the trade name BC454, which provides a unique signature for neutrons that have deposited all their energy within the detector.[4] Because the scintillator material is solid plastic, its efficiency at high energies is much greater than that of gas proportional counters, and it is more rugged and stable than liquid scintillators. The prototype detector is large enough to provide a reasonable counting rate, and much of the hardware and software is readily adaptable to field use. Data acquisition can be controlled using an interface to a portable personal computer, and the final analysis can be performed on a transportable computer workstation. Previous reports document the detector's use for identifying enriched uranium by neutron-induced fission,[5] for counting warheads on silo-based missiles,[6] and for measuring far-field fluxes from a nuclear reactor.[7]

Present Experiment. An opportunity to test the prototype boron-loaded spectrometer with realistic mockups of nuclear warheads arose in connection with a Defense Advanced Research Projects Agency (DARPA) program to develop imaging techniques for radioactive sources. LANL's Advanced Nuclear Technology Group provided different types of mockups, and spectral measurements were made over several days. Because the prototype instrument was essentially uncalibrated and no analysis software had yet been written, only the on-line measurements have been previously available. Subsequent software development has allowed us to produce a series of reports as support for a portable version of the instrument, the Field Neutron Spectrometer (FNS).

* Bicron Corp., 12345 Kinsman Rd., Newbury, OH 44065

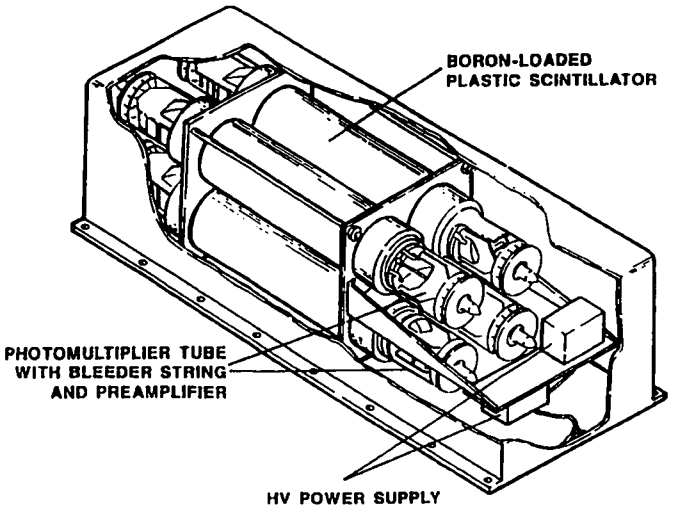

Fig. 2.1. Cutaway view of the neutron spectrometer. Four scintillator rods, each with two photomultiplier tubes, indicate the direction of the incident neutron flux. Most of the electronic components are contained in a separate package (not shown).

Scope of this Report. Section 2 uses calibration measurements to explain the detector's operating principles, and Sec. 3 uses measurements on ^{252}Cf and ^{240}Pu sources to develop an analysis procedure for identifying neutron sources. Although not emphasized in this report, the four-element segmentation of the prototype detector also allows estimates of the source direction and the background from room scattering. This extended capability is discussed in a separate paper,[8] which will be referred to as needed. Later reports will discuss the design characteristics of the warhead mockups, calculations of the expected energy spectra, and comparisons between the measurements and calculations.

2. BASIC DETECTOR PRINCIPLES

Overview. The operation of the detector provides three advantages over traditional proton-recoil spectrometers: (1) Neutron events are identified unambiguously and non-neutron backgrounds are completely eliminated; (2) built-in test and calibration functions help to ensure the reliability of the measurements; and (3) the incident energies for neutrons from 0.5–10 MeV can be determined with good resolution and without unfolding. These features are direct consequences of the instrument's unique scatter-and-capture detection mechanism, which selects only fast neutrons that deposit essentially all their energy in *n-p* scattering and are then captured by the boron. This section explains the connections between the three operational advantages and this basic process.

Detector Layout. As shown in **Fig. 2.1**, the instrument head consists of four BC454 scintillator rods with photomultiplier tubes at each end, as well as two high-voltage power supplies and four separate preamplifier chains.[9] A second package contains the gated integrators, timing logic, command microprocessor, and 1-Mbyte onboard memory. A third unit provides the interface between the processor and a personal computer. The four side-by-side scintillator elements (Rods 1 and 2 toward the front, Rods 3 and 4 toward the rear) also indicate the direction of the incident neutron flux. Thus, the instrument actually provides two types of neutron information, spectroscopy and directionality.

Time-Difference Spectrum. The *first* feature of the scatter-and-capture process is based on the time difference T between the first and second interactions that define a desired coincidence event. These differences are measured by a clock in the electronics and recorded as a spectrum of count rate versus time. **Figure 2.2** illustrates the analysis of a time spectrum measured with an unshielded laboratory ^{252}Cf source, which was located 54 cm to the side of the detector and facing a pair of vertical rods. For this measurement with a low-intensity source (Run 802 in the experiment log), the total collection time was 7.25 h. On the logarithmic plot, the open circles show the measured count rates in two important regions of the time spectrum ("EARLY" and "LATE"). Because the capture cross section varies inversely with velocity ($1/v$), the capture events should have a distribution of time differences with an exponential shape $R(T) \propto \exp(-T/\tau)$. Given the amount of boron in our scintillator (1% ^{10}B by weight), the decay constant τ should be about 2 μs.[9] At longer times, perhaps five time constants, the neutron has either been captured or has escaped, and all events are random coincidences produced by uncorrelated gamma-ray or neutron interactions. Subtracting this "random background" from the raw data gives a corrected result ("subtd data") that agrees well with the expected 2.3-μs decay curve. Alternatively, the "predicted rate" obtained by adding the 2.3-μs curve to the random background reproduces the raw data inside both the EARLY and LATE time windows. The agreement between the data and predictions demonstrates the first signature of fast-neutron capture in the detector, the exponential time dependence of the capture time-interval values. The subtraction of events in the EARLY and LATE windows exploits this time dependence to provide the instrument's excellent background rejection.

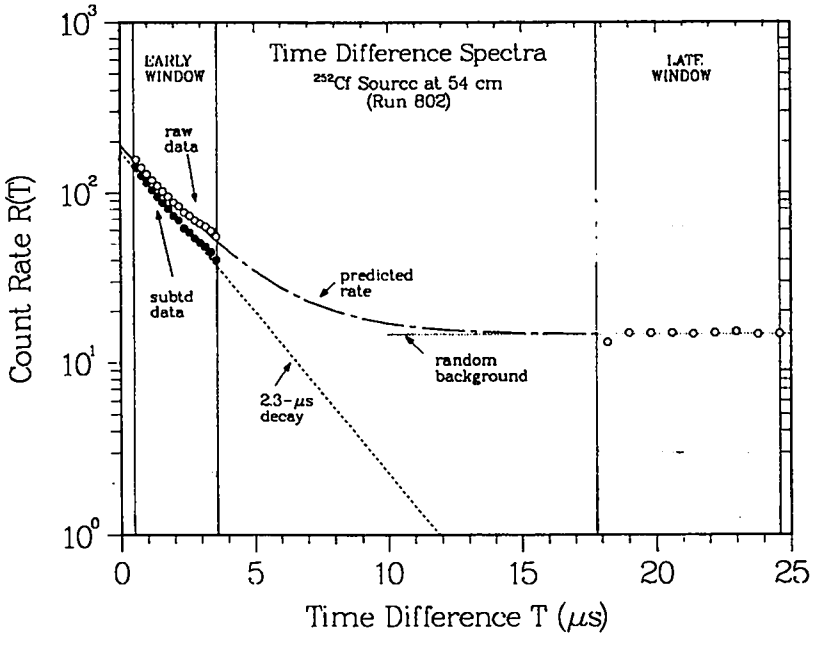

Fig. 2.2. Analysis of a time-difference spectrum measured with a laboratory ^{252}Cf source placed 54 cm from the detector. The EARLY and LATE windows are used to select two sets of events for further processing. In these windows the raw data are either neutron scatter-and-capture events (the 2.3-μs line) or random coincidences (the constant level).

Dead-Time Corrections. Another use for the time-difference spectrum involves the correction for dead time in the measurements. As discussed in Ref. 9, after receiving a first pulse (*S1*), the electronics wait a fixed time T_o of about 30.5 μs for the detection of a second pulse (*S2*). During this fixed time, any additional *S1* pulses are ignored. At the end of the delay, information for the event is transferred to a buffer for further processing. A straightforward type of dead time occurs if this buffer fills at high data rates, because no other events can be recorded until it is emptied. Although a correction can be estimated to account for these buffer overflows, its reliability is low because the emptying time depends on the mixture of events (single pulses, coincidences, and multiple-rod hits). For the present experiment, however, these overflows are a potential problem only at the highest rate (Run 817 in the experiment logs). The other dead-time corrections correspond to missed *S1* or *S2* pulses. A minor problem is missed *S2* pulses, because the electronics are gated off for 0.3 μs after each *S1* pulse to avoid after-pulsing in the preamplifiers. A larger concern is *S1* pulses that are missed because of the nonparalyzable dead time of the fixed 30-μs delay. A correction for this effect is automatically calculated from the time delay T_o and the estimated singles rate R_s. The approach is summarized in **Fig. 2.3**, which compares the relationship between the true (R_t) and observed (R_s) rates with the prediction $R_s = R_t/(1 + R_tT_o)$ obtained from an analytical model for nonparalyzable systems.[10] For the ^{252}Cf calibration run, the rate was 746 counts/s and the correction was only 2.3%; the point at the highest rate, R_s = 3926 Hz, has a dead-time correction of 10.7% (including buffer overflows). At the highest rates, the random background in Fig. 2.2 is not a constant; missing *S2* pulses give it an increasing slope.[10] Because this slope would cause an undersubtraction of the random background, an additional dead-time correction is automatically included.

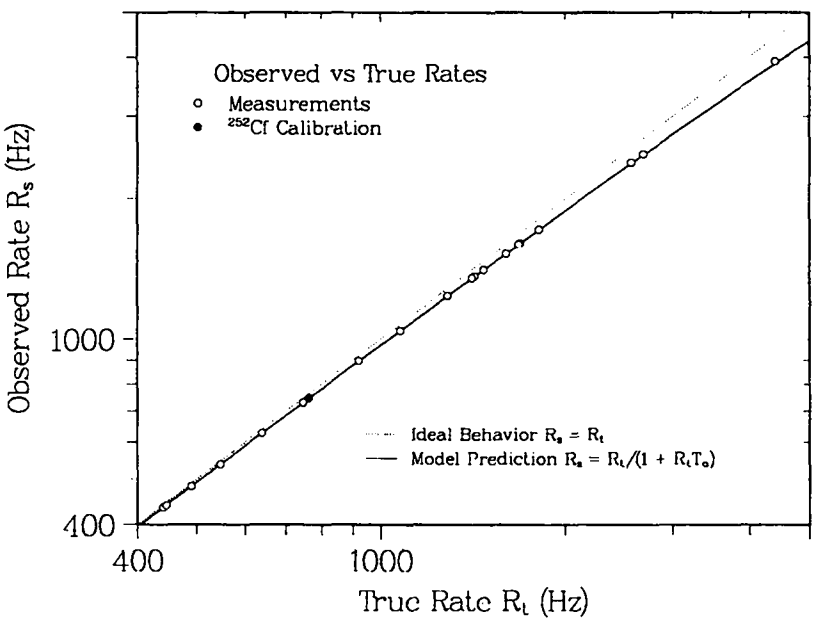

Fig. 2.3. Dead-time corrections. An ideal counter would operate with no dead time, i.e., the true and measured rates would be the same ($R_s = R_t$; dotted line). The actual detector misses some counts because of dead time; the correction calculated by the software agrees well with predictions from a simple model.

Pulse-Height Distributions. Further analysis of the data includes only those events with second pulses in the two time windows shown in Fig. 2.2. Separate *S2* spectra are accumulated for each region; as in the time spectrum, their subtraction gives a background-corrected result that should reflect only the true scatter-and-capture coincidences. **Figure 2.4a** shows the *S2* spectrum for the ^{252}Cf measurement in Fig. 2.2; it has been summed over all four rods and plotted on a scale calibrated in keV$_{ee}$, meaning "keV electron equivalent." This light-output scale is needed because energy conversion in scintillators saturates and becomes nonlinear at the high energy densities produced by slower or heavier particles, such as our low-energy recoil protons. Because energetic electrons are the least-ionizing particles—and their response is the most linear—the pulse heights for other particles are conventionally expressed in units of electron energy, hence, keV$_{ee}$. Measurements of Compton electron spectra from gamma rays at different energies are usually used to establish this scale. In our case, the reaction products from the boron capture itself provide an internal calibration source for the instrument.

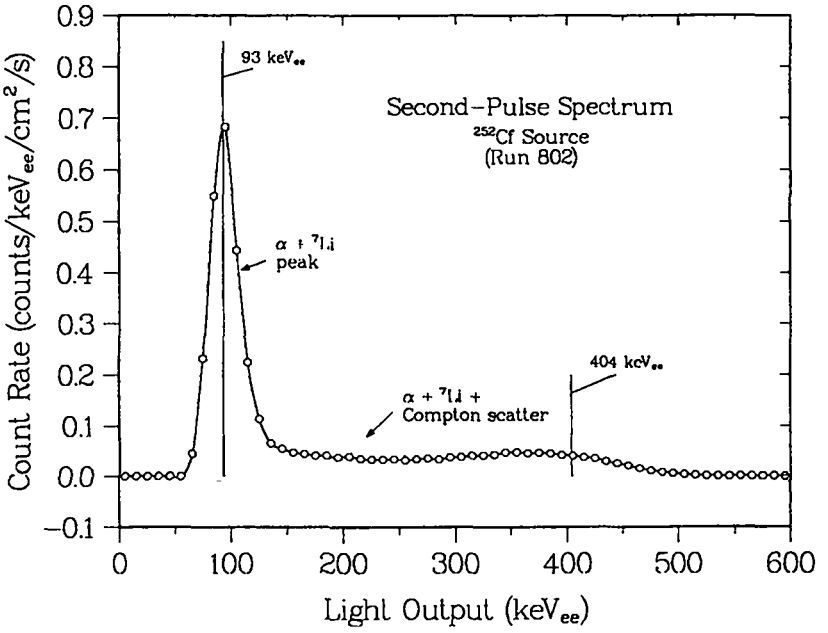

Fig. 2.4a. Pulse-height spectrum for events with second (*S2*) pulses in the EARLY and LATE time windows indicated in Fig. 2.2. Separate spectra for the two windows have been subtracted to produce a background-free spectrum, which illustrates the definite structure associated with the ^{10}B(n,α)^{7}Li reaction.

Second-Pulse Spectra. The *S2* spectrum is responsible for the *second* important advantage of the scatter-and-capture process. The ^{10}B(n,α)^{7}Li capture reaction almost always produces a 1.5-MeV alpha particle, a 0.8-MeV ^{7}Li ion, and a 478-keV gamma ray for the decay of ^{7}Li from its first excited state to the ground state. The energies of the recoiling alpha and ^{7}Li particles are instantly absorbed, but they produce only 93 keV$_{ee}$ of light because of the saturation in the energy-to-light conversion. If the 478-keV gamma ray undergoes Compton scattering before escaping, it can deposit an additional energy of up to 311 keV. Thus, in Fig. 2.4a the 93-keV$_{ee}$ peak corresponds to detection of only the

recoil alpha and ^{7}Li ions, with complete escape of the gamma ray; the long shoulder results from adding a fraction of the 311 keV from the recoil electron, which produces a shifted Compton edge at (311 + 93 = 404) keV$_{ee}$. Resolution and multiple-scattering effects place the location of this edge about midway between the maximum and half-maximum of the shifted Compton distribution. In Fig. 2.4a the vertical lines at 93 keV$_{ee}$ and 404 keV$_{ee}$ mark the locations of these two specific features, the recoil peak and Compton edge, which establish the gain and offset for the light-output scale. The definite shape of the *S2* spectrum not only adds a second criterion for neutron selection, it also establishes a valuable internal gain calibration for the detector.

Accidental Subtraction. The *S2* spectrum also allows a check on the subtraction of random backgrounds and the associated dead-time correction. Neutron-capture events cannot give light outputs above 500–600 keV$_{ee}$; in fact, very few true coincidences of any type can produce signals at these energies. To focus on this region, **Fig. 2.4b** shows the *S2* spectrum on an expanded scale. Problems with background subtraction would appear as an overall offset from zero; for example, leaving out the *S2* dead-time correction would cause a positive offset. Also, a particular type of pileup can occur at very high count rates, as follows. In the EARLY *S2* window, the overshoot from the tail of the immediately preceding *S1* pulse can cause a small negative baseline shift for the *S2* pulse; there is no corresponding shift for the well-separated *S2* pulses in the LATE window. As a result, the *S2* subtraction often results in several slightly negative channels just above the Compton edge, which shows up as a small negative integral at high pulse heights. For the spectrum shown, this effect is barely apparent at 600–800 keV$_{ee}$; the integral from 600–2400 keV$_{ee}$ is $-3.7 \pm 2.0 \times 10^{-5}$ counts/cm^2/s, which is negative but still consistent with zero. In any case, this offset has no direct effect on the instrument's efficiency or spectroscopy, both of which depend primarily on the size of the *S1* pulse.

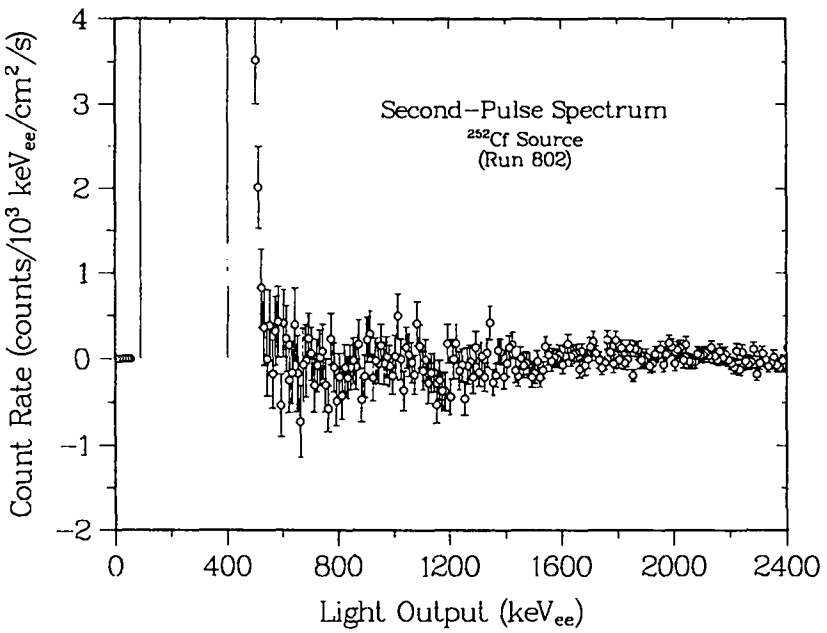

Fig. 2.4b. *S2* spectrum from Fig. 2.4a, shown on an expanded scale. Correct accidental subtraction should give a zero integral over the region from 600–2400 keV$_{ee}$.

Realistic Example. Figures 2.2 and 2.4 have demonstrated the excellent neutron selection obtained in the favorable situation of a long measurement with a calibration source located very near the detector, that is, for very little scattered background. To illustrate the background rejection under less favorable conditions, we now show the corresponding results from a measurement with an "unknown" distributed source located at a large distance (Run 812 in the experiment log). **Figure 2.5a** shows the time-difference plot, which indicates that this measurement involves a coincident neutron flux that is about 1/30 of that for the ^{252}Cf calibration shown in Fig. 2.2. The random background, however, is reduced by only about a factor of 8; that is, its level relative to the signal has increased almost fourfold. Nevertheless, within the EARLY time window the subtracted data is still well described by the 2.3-μs decay curve expected for scatter-and-capture events. The second requirement for neutron events, the characteristic *S2* spectrum, is shown in **Fig. 2.5b**. The capture signature stands out clearly, with the peak and shifted Compton edge both located at the required positions, at least within the statistical uncertainties.

S1 Difference Spectra. The instrument's *third* and perhaps primary advantage is its capability for determining the energy of the incident neutrons, at least over the range most important for fission neutrons, roughly 0.5–10 MeV.[9] This feature results from the coincidence requirement that connects the two major techniques for neutron detection, elastic scattering at high energies ($E_n > 0.5$ MeV) and capture reactions at low energies ($E_n < 0.1$ MeV). Only fast neutrons can produce a first pulse, and only those that have subsequently deposited most of their energy in the scintillator can produce a second pulse. Thus, observation of the sequential pair of pulses ensures that the pulse-height spectrum for the first pulse (*S1*) is directly related to the spectrum of incident neutron energies E_n. First, as with the *S2* spectra, non-neutron contributions to the *S1* spectrum are removed by subtracting events whose *S2* pulses fall in the LATE window from those in the EARLY window. Next, two relatively simple conversions are required to transform the measured pulse heights into a spectrum of incident neutron energies. We first correct each pulse-height value for the saturation in the scintillator's energy-to-light conversion, which changes the electron-energy scale in keV$_{ee}$ into a scale for neutron energy in MeV.[9] Next, we divide this spectrum energy-by-energy by a calculated neutron-detection efficiency,[9] which provides the absolute flux distribution dN/dE as a function of neutron energy E_n. Because the connection between the *S1* and *S2* electronics is fixed, we can correct for gain shifts by simply changing an off-line software parameter to place the *S2* recoil peak and Compton edge at the specified locations.

Energy Measurements. For our ^{252}Cf calibration, the corrected spectrum for the two rods facing the source is shown in **Fig. 2.6**. Several features can be pointed out. First, the useful response of the system extends from about 0.75 to 10 MeV, or at most from 0.5–15 MeV. The correction for detection efficiency becomes questionable at higher energies, and saturation causes proton recoils from lower-energy neutrons to produce too little scintillation light (note the cutoff below 0.5 MeV). Second, the count rate for fission spectra falls by a factor of 250–1000 from 1 to 10 MeV, which severely limits the statistical precision at higher energies. Third, the measured spectrum shows some clear differences from the expected ^{252}Cf distributions obtained from a recent evaluation.[11] In particular, the structure near 3 MeV is associated with a switchover between two different amplifier-integrator pairs, and the measurements at high energies are consistently lower than the expected values. The discussion of these differences occupies most of the following section.

Review. This section has emphasized three important features that result from applying the sequential-pulse requirement to the scatter-and-capture process for fast-neutron interactions in borated-plastic scintillators. The time-difference plot provides reliable corrections for all types of backgrounds, regardless of their source. The characteristic *S2* spectrum provides an accurate internal energy-loss calibration. Together, the time-difference

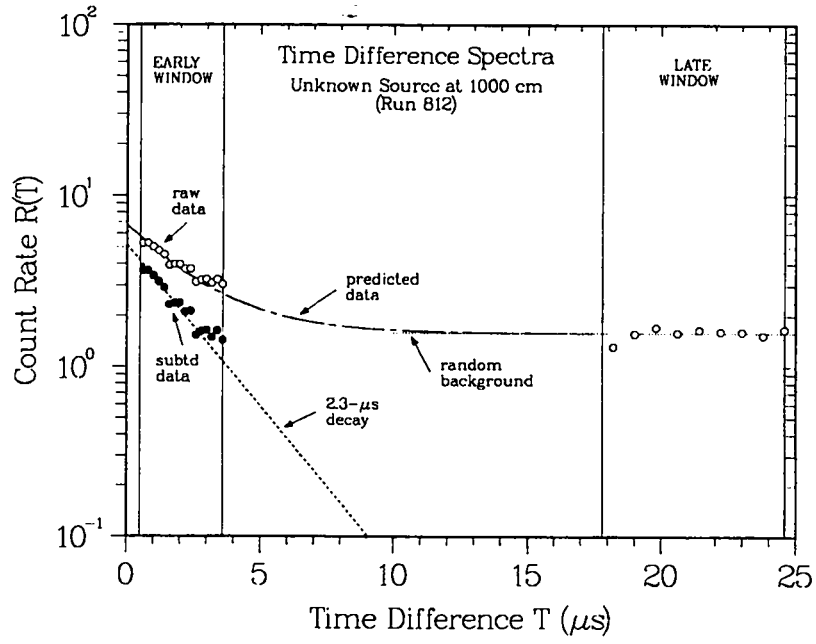

Fig. 2.5a. Time-difference plot for an unknown source (compare with Fig. 2.2).

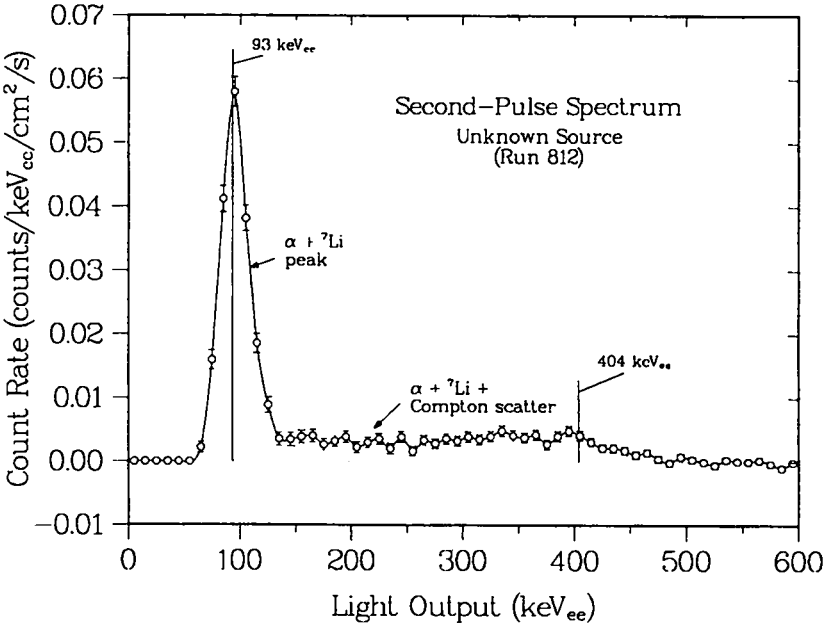

Fig. 2.5b. Second-pulse (*S2*) plots for an unknown source (compare with Fig. 2.4a).

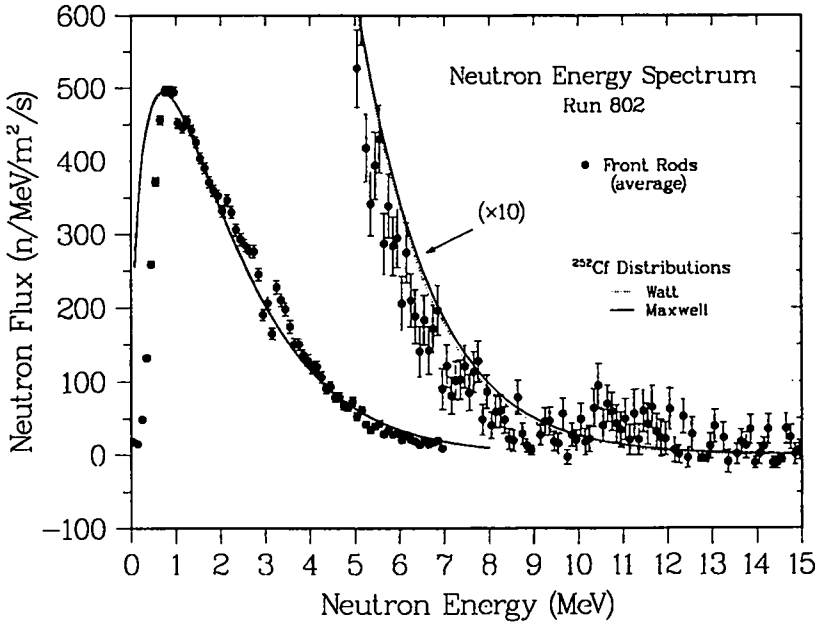

Fig. 2.6. Neutron flux spectrum obtained from the first pulse (*S1*) after corrections for energy-loss saturation and detection efficiency. Comparison shows fair agreement with the expected ^{252}Cf distributions.[11]

and second-pulse requirements provide unambiguous neutron identification and reliable energy calibration. On this basis, the proton-recoil energy provided by the *S1* pulse can be used to generate an event-by-event energy measurement for incident neutrons, which allows neutron spectroscopy without complex unfolding.

3. SPECTRAL ANALYSIS

Overview. In the complete analysis of the data, the multielement segmentation of the detector is used to determine the direction of the incident neutron flux, estimate the amount of room-scattered background, and correct the energy spectrum by subtracting an estimated background. Such directional information is not an important issue for the present measurements, which were all made in a low-scattering environment (so the background corrections are small) and with the source placed directly in front of the detector (so the incident angles are known). For the clarity of the present discussion, we will simply adopt the background-subtracted spectra and state that the corrections are either negligible or very small, especially for the calibration runs discussed here. A companion report[8] discusses these directional analyses. This section will concentrate on comparing the calibrations with evaluations, correcting the spectra for instrumental problems, and expressing the shape information in terms of a few simple parameters.

^{252}Cf Distributions. Because the energy distribution of neutrons from the spontaneous fission of ^{252}Cf is very well known,[11] this calibration provides a definitive test of the detector's ability to provide absolute spectral measurements. In **Fig. 3.1**, the final background-corrected data are shown as open circles, with the errors omitted for clarity.

To improve the statistical accuracy, the data have also been averaged over logarithmic energy intervals to provide the compressed data set shown as solid circles. The two curves were shown earlier on a linear scale in Fig. 2.6; they are from the recent evaluation in Ref. 11. The most accurate result is the Watt spectrum (dashed line), although an approximate Maxwell distribution (solid line) with a temperature parameter of 1.42 MeV is very similar (within 10% below 10 MeV). The important point is that there is a significant discrepancy between the measurements and either of the evaluations. Although this deviation could signal a breakdown in the simple assumptions about energy-to-light conversion and detection efficiency, we will assume it indicates a problem associated with the early instrument used for these measurements. Because the discrepancy in the measurements is much larger than the difference between the two evaluations, our analysis will emphasize the convenient analytical form of the Maxwell distribution. On this basis, we will use the ^{252}Cf measurement to develop an empirical correction to the calculated detection efficiency, which will then be crosschecked against a separate calibration with a ^{240}Pu source.

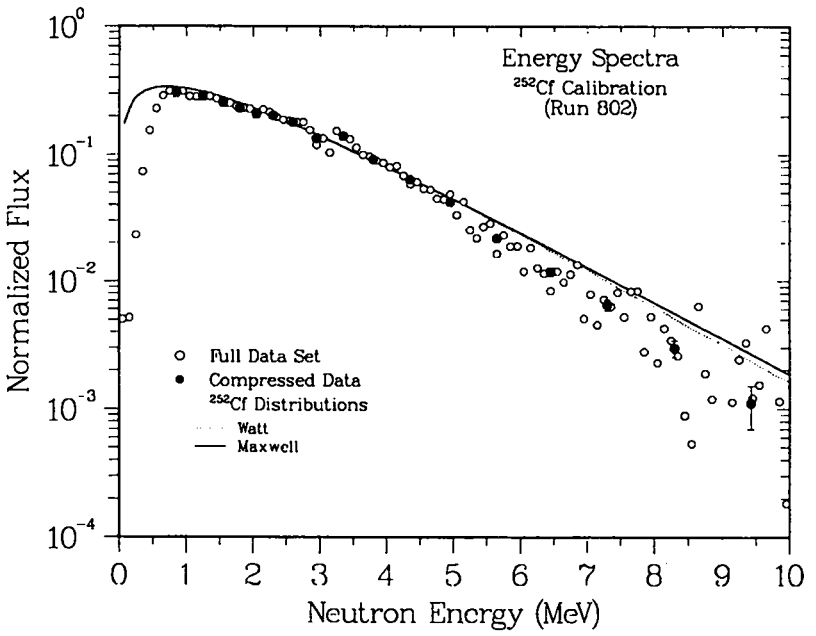

Fig. 3.1. Comparison between normalized ^{252}Cf measurements and evaluated energy distributions. The open circles are the background-subtracted data; the closed circles are the data averaged over logarithmic energy bins to improve the statistical accuracy. The data are normalized to Maxwell distributions with unit area. The curves show two alternative evaluations.

Maxwell Formalism. For a Maxwell flux function normalized to unit area, the energy dependence is given in terms of a single parameter, the average temperature T, as follows:

$$M(E) = \frac{2}{\sqrt{\pi} T^{3/2}} E^{1/2} e^{-E/T} \ .$$

Because our measurements are stated as absolute neutron flux in neutrons/m^2/s, it is convenient to define a new distribution that includes a scaling parameter A that equals the integrated flux over all energies:

$$N(E) = \frac{2A}{\sqrt{\pi}T^{3/2}} E^{1/2} e^{-E/T} .$$

This function suggests a transformation

$$O(E) = \ln\Big(N(E)E^{-1/2}\Big) = \ln\Big(\frac{2A}{\sqrt{\pi}T^{3/2}}\Big) - E/T ,$$

which is a line $y = a + bx$ whose slope b gives the temperature value $T = 1/b$ and whose intercept a gives the energy-integrated flux A:

$$A = \frac{\sqrt{\pi}}{2} T^{3/2} e^{a} .$$

Finally, to emphasize the difference in slopes for different measurements we define a simple function

$$P(E) = O(E) - a = -E/T ,$$

which includes only the temperature T.

Temperature Correction. The fitting procedure is illustrated by **Fig. 3.2**, which shows $P(E)$ functions for the two calibration runs with ^{252}Cf and ^{240}Pu sources. The transformed ^{252}Cf calibration is the measurement shown in the previous figures. The ^{240}Pu calibration was made using a bare nonweapon source at a distance of 150 cm (Run 612 in the experiment log). The two lines in the figure show the transformed Maxwell functions over the region included in the fitting, 0.75–10.0 MeV. Because of the clearly nonstatistical errors in the data, the uncertainties in the temperature values are obtained not from the statistical errors on the measurements but from the errors in the linear correlation coefficients. As implied by Fig. 3.1, the temperature $T = 1.25 \pm 0.03$ MeV for the ^{252}Cf spectrum is much lower—by 0.17 MeV—than the accepted Maxwell value of $T_M = 1.42$ MeV.[11] Similarly, the T-value of 1.00 MeV for the ^{240}Pu measurement is 0.19 MeV below a published value of 1.19 MeV.[12,13] This systematic offset suggests that the efficiency should be corrected by an exponential of the form $F(E) = e^{E/T_F}$, with T_F given by the equation

$$T_F = \frac{T_M T}{(T_M - T)} .$$

To obtain the desired value of $T_M = 1.42$ MeV, a measured ^{252}Cf distribution with $T = 1.25$ MeV requires an exponential correction with $T_F = 10 \pm 2$ MeV. As a check, applying this correction to the ^{240}Pu data shifts the temperature to $T = 1.1 \pm 0.2$ MeV, which is in good agreement with the published value.

Energy-Dependent Deviations. Multiplying the efficiency by the exponential correction $F(E)$ provides the correct temperatures and therefore remedies the rapid falloff of the data at high energies. As seen in Fig. 3.2, however, there remains a problem with residual deviations from the expected Maxwell energy dependence. As with the temperature discrepancy, an instrumental origin for the deviations is suggested by the similarity of their behaviors for the two calibration measurements. This observation is emphasized in **Fig. 3.3**, which shows the ratio between the measurements and the fitted Maxwell distributions. To obtain the most accurate energy-dependent correction, we calculated this ratio

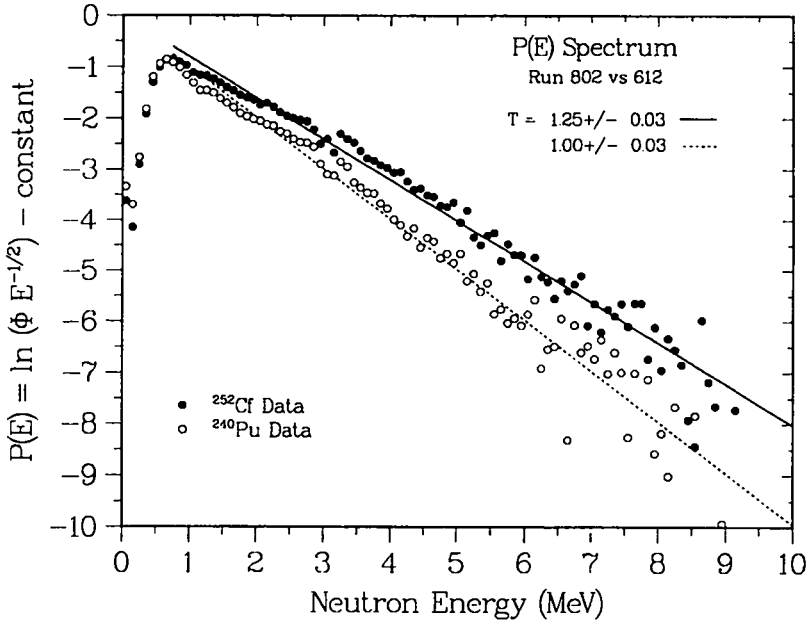

Fig. 3.2. Maxwell fits to the measured calibration spectra as transformed to $P(E)$ functions to emphasize the slopes of the distributions. The two temperatures are consistently lower than the expected values.

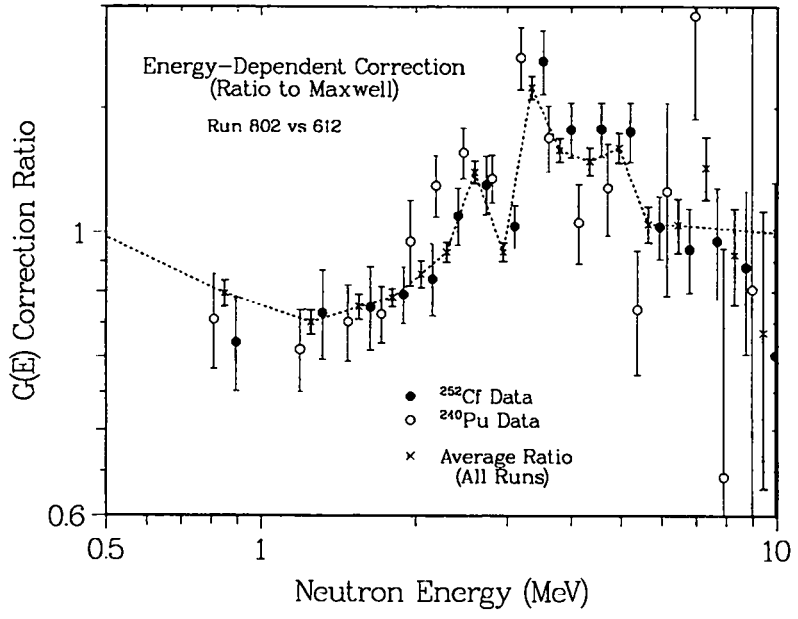

Fig. 3.3. Deviations between the measurements and Maxwell distributions. The open and closed circles show ratios between the calibrations and the fitted Maxwell distributions. The dashed line connects values for the average deviation for all the measurements, which provides an estimated instrumental correction $G(E)$.

for all the measurements and averaged the values to provide a ratio-to-Maxwell correction $G(E)$, which is shown by the set of points and the dashed line. In this correction, the overall variation is probably associated with nonexponential efficiency errors, while the sharp change near 3 MeV reflects a localized hardware problem. Above 6–7 MeV, the corrections are not statistically significant and have been extrapolated to give a value of 1.0 at 10 MeV.

Corrected Measurements. **Figure 3.4** shows the effect on the transformed $P(E)$ distributions of applying both the $F(E)$ temperature and $G(E)$ energy-dependent corrections to the calibration runs and then refitting the data. The average temperatures have shifted to the expected values, and most of the localized structure has disappeared. **Figure 3.5a** repeats the comparison, this time showing the corrected but untransformed $M(E)$ distributions for comparison with the original distribution shown in Fig. 3.1. This comparison clearly emphasizes the significance of the differences between the count rates near the peak at 1–2 MeV and in the exponential region at higher energies. **Figure 3.5b** shows the ratio-to-Maxwell results for the corrected distributions; the deviations from unity are now comparable with the statistical errors. In addition, the solid line presents the ratio between the evaluated Watt and Maxwell ^{252}Cf distributions shown in Fig. 3.1. Even with the good statistics of the relatively lengthy calibration runs, the differences between the two evaluations are completely negligible.

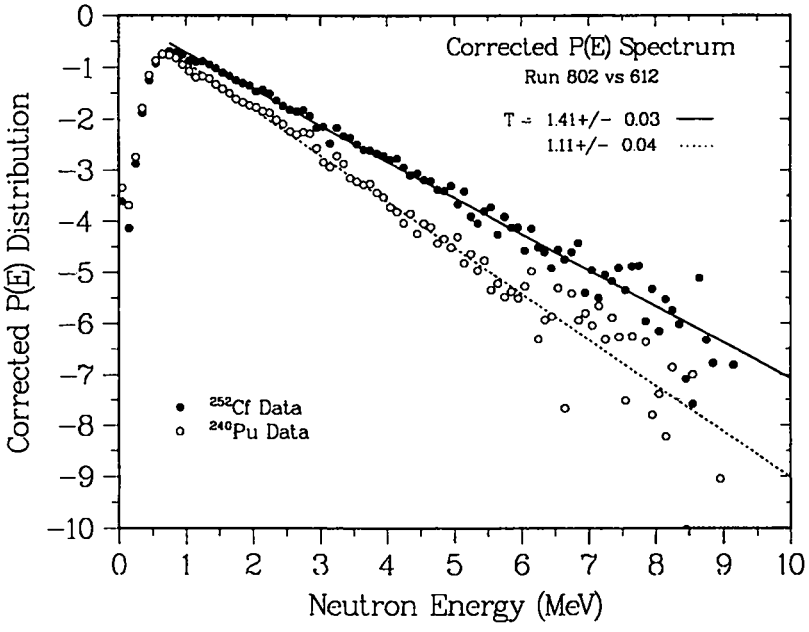

Fig. 3.4. Transformed $P(E)$ distributions corresponding to those shown in Fig. 3.2, but now using a modified efficiency function that includes the exponential and energy-dependent corrections.

Fitting Parameters. As in the analysis of the original data, the Maxwell analysis for the corrected measurements expresses the shape information in terms of a few simple parameters: (1) the detector flux in neutrons/m^2/s, from the intercept; (2) the average slope of the exponential falloff, from the temperature; and (3) the deviations from this average slope, such as the ratio plots or, even better, the centroids and widths from a moment analysis of these ratios. The parameters from the Maxwell analysis are collected in **Table I**, along with several quantities that describe the on-line measurements (run times,

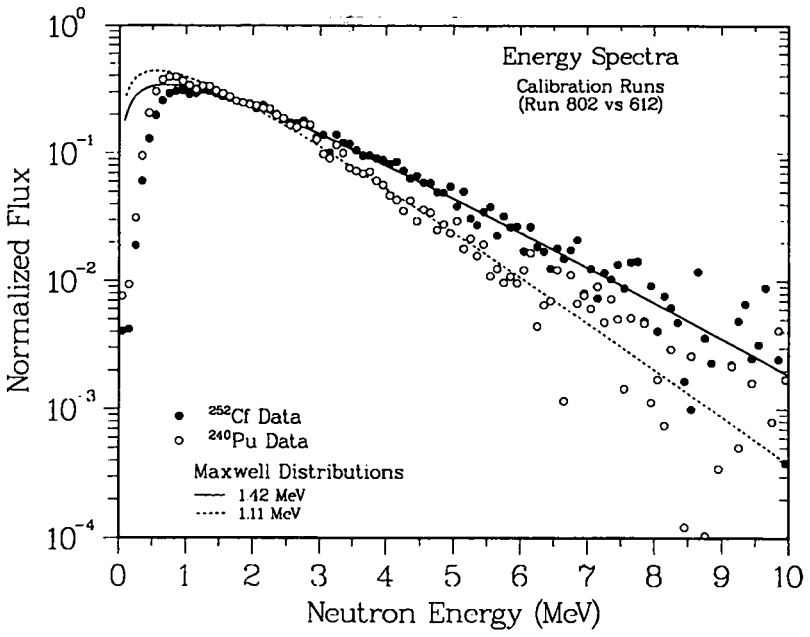

Fig. 3.5a. Corrected but untransformed $M(E)$ distributions corresponding to the original ^{252}Cf distribution shown in Fig. 3.1, but now including the exponential and energy-dependent corrections.

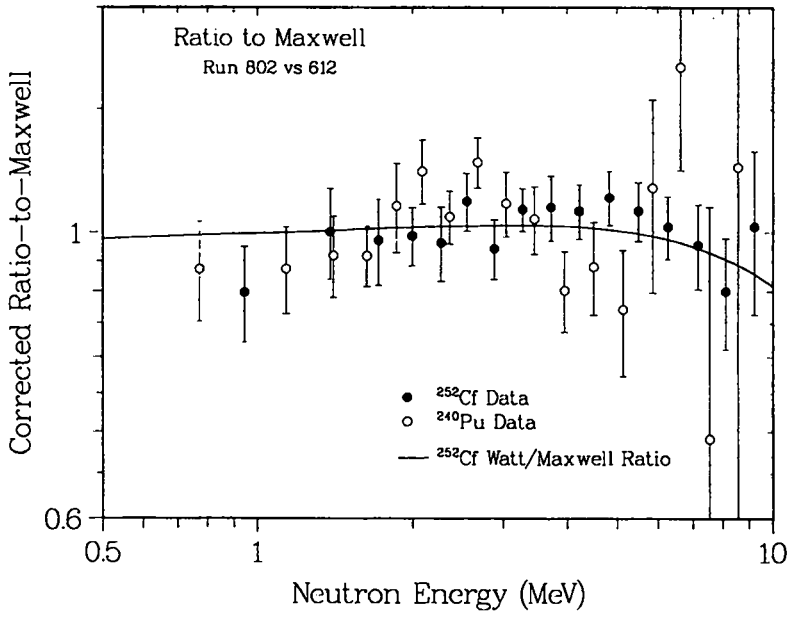

Fig. 3.5b. Ratio-to-Maxwell plots for the corrected measurements in Fig. 3.5a. For comparison, the solid line indicates the ratio between the Watt and Maxwell evaluations shown in Fig. 3.1.

TABLE I: Measurement Parameters

This table summarizes the information for the analyses of the different sets of measurements. The notation is as follows:

On-line Quantities

J Index (1–22) for each set of runs. Similar runs are grouped together.
RUN First run in the original set of run numbers. For example, Run 802 is Runs 82–83; Run 612 is the sum of Runs 612–618.
NAME Mnemonic for the particular source, taken from the run logs.
DIST Distance (cm) between source and detector, from the run logs.
TIME Measurement time interval (min), calculated by conversion of the number of 96-s frames of event data into time in minutes.
RATE Singles rate (Hz) from the off-line analysis code.
DTM Estimated dead-time fraction from the analysis code.

Off-line Quantities

FLXS Background-subtracted flux integral and percentage error.
SOUS Total source emission at all angles, in units of 10^5 neutrons/s, obtained by correcting FLXS for solid angle using DIST.
TMPS Temperature from the Maxwell fit to the corrected spectrum.
NRMS Normalization factor from the y-intercept of the Maxwell fit to the corrected spectrum. It has been multiplied by 10^4 for numerical comparison with FLXS in neutrons/m^2/s.
SCAS Scale factor for the fraction of the corrected flux in the energy range 0.75–10.0 MeV. This factor was used to convert the measured integral for the data to give the FLXS value for all energies.
CH2S Reduced chi-square (χ^2/N) for Maxwell fit to the subtracted spectrum.
CH2C χ^2/N for agreement with the ^{252}Cf measurement.
CH2P χ^2/N for agreement with the ^{240}Pu measurement.

```
  J RUN  NAME  DIST TIME RATE   DTM
               cm   min ct/s   frac
 20 612   PU    150  160 1363 0.0415
       FLXS   SOUS
       5802  1.641
+/-     1.5    1.5
       TMPS   NRMS   SCAS
       1.11   5767  0.695
       0.04
       CH2S  CH2C  CH2P
  fit   1.3  20.0   0.0

  J RUN  NAME  DIST TIME RATE   DTM
               cm   min ct/s   frac
 21 802 CF252   55  435  746 0.0228
       FLXS   SOUS
       2614  0.099
+/-     1.3    1.3
       TMPS   NRMS   SCAS
       1.41   2611  0.766
       0.03
       CH2S  CH2C  CH2P
  fit   1.3   0.0  25.8
```

source distances, dead times, etc.). The intercept values give normalized areas (NRMS in the table) of 2611 and 5767 n/m^2/s for the ^{252}Cf and ^{240}Pu measurements, respectively. For comparison, the fitted T-values (TMPS) can be used to calculate the fraction of the yield inside the measured 0.75–10.0 MeV energy range (SCAS = 77% for ^{252}Cf and 70% for ^{240}Pu); correcting the measured integrals by these values gives estimated total fluxes (FLXS) of 2614±1.3% n/m^2/s (^{252}Cf) and 5802±1.5% n/m^2/s (^{240}Pu), in good agreement with the fitted intercept values. The source distance (DIST) can be used to convert these total fluxes into source emission rates (SOUS, in neutrons/s). Finally, a simple expression of the deviations from the standard Maxwell shape is provided by the three chi-square values included in the table. The CH2S value is the reduced chi-square from the corrected Maxwell fit; it should approach 1.0 for bare sources. The CH2C and CH2P values refer to the deviations between a particular measurement and the two calibrations; the values of 20.0 and 25.8 reflect the large difference between the two calibration spectra.

Summary. It is important to remember that the corrections for temperature and energy dependence are required only to obtain the proper *absolute* spectral shapes. Even without the corrections, as in Figs. 3.1–3.2, the *relative* difference between the neutron sources is clear. As a practical matter, the usefulness of the spectral measurements depends mainly on their *reproducibility* and *distinguishability*. In this view, the calibration check provided by the *S2* spectrum in Sec. 1 establishes the reproducibility, and the original comparison between the ^{252}Cf and ^{240}Pu spectra demonstrates the necessary distinguishability. Simply put, the corrections that provide the absolute distributions in Fig. 3.5a make it easier to recognize trends in the measurements, and the Maxwell analyses are a convenient framework for determining parameters such as the intensity, average slope, and deviations from the standard shape. The eventual significance of the absolute corrections will depend on their usefulness for realistic sources in particular scenarios.

4. CONCLUSIONS AND FUTURE WORK

This report supplements the original publication's technical explanation[9] with a discussion of the practical significance of measurements of time differences, neutron-capture pulse heights, and proton-recoil energies. As discussed in Sec. 2, these measurements provide the background correction, energy-loss calibration, and neutron-energy spectra that lead to the advantages of boron-loaded scintillators over other neutron detectors. Although an additional empirical correction was needed to obtain the correct absolute spectra, its results in Sec. 3 are impressive: the measured ^{252}Cf and ^{240}Pu spectra agree with the expected Maxwell distributions, and their shapes are easily distinguishable. In practice, however, absolute spectra may not be the issue; reproducible relative measurements may be sufficient for locating or identifying neutron sources, especially if benchmarks are available. Thus, the real indication of the detector's usefulness depends on the future analysis of measurements and calculations for the complete set of weapon mockups. The goal of this analysis will be to associate intensities, temperatures, and non-Maxwell spectral features with the structure and materials of particular neutron sources.

Omitted from this report is a discussion of the directionality and background subtraction made possible by the detector's multielement segmentation. These capabilities were originally recognized and developed by computer simulations for fast-neutron detectors in Ref. 14, and the present data set provides the first test of the concept for measurements on distributed sources at different distances. A companion report[8] describes the additional analysis algorithms, the accuracy of the source location, and the usefulness of the technique in establishing the existence of a radiation source in the presence of background radiation.

ACKNOWLEDGMENTS

These measurements would have been impossible without the support of LANL's Advanced Nuclear Technology Group. Marilyn Halbig of Space Data Systems adapted the spacecraft software for use with the backup instrument. Calvin Moss and Darrell Drake of Astrophysics and Radiation Measurements and Bill Urban of Applied Theoretical Physics provided valuable discussions and comments about the manuscript.

REFERENCES

1. W. C. Sailor and S. G. Prussin, "A Model for Electron/Ion Recombination in Ionization Chambers," *Nuclear Instruments and Methods* **A274**, 305–313 (1989).
2. K.-H. Beimer, G. Nyman, and O. Tengblad, "Response Function for ^{3}He Neutron Spectrometers," *Nuclear Instruments and Methods* **A245**, 402–414 (1986).
3. L. J. Perkins and M. C. Scott, "The Application of Pulse-Shape Discrimination in NE 213 to Neutron Spectroscopy," *Nuclear Instruments and Methods* **166**, 451–464 (1979).
4. D. D. Drake, W. C. Feldman, and C. Hurlbut, "New Electronically Black Neutron Detectors," *Nuclear Instruments and Methods* **A247**, 576–582 (1986).
5. C. E. Moss, R. C. Byrd, G. F. Auchampaugh, and W. C. Feldman, G. P. Estes, R. I. Ewing, and K. W. Marlow, "Detection of Uranium-Based Nuclear Weapons Using Neutron-Induced Fission" (submitted to *IEEE Transactions on Nuclear Science*).
6. R. C. Byrd, G. F. Auchampaugh, C. E. Moss, and W. C. Feldman, "Warhead Counting Using Neutron Scintillators: Detector Development, Testing, and Demonstration," *IEEE Transactions on Nuclear Science* **NS-39**, 1051–1055 (August 1992).
7. Paul Whalen *et al.*, "Measurements and Calculations of Neutron Energy Spectra for the Radiation Environments Program," Los Alamos National Laboratory report (in preparation).
8. Roger Byrd, George Auchampaugh, and William Feldman, "Directional Measurements for Sources of Fission Neutrons," Los Alamos National Laboratory report LA-12633-MS (in preparation).
9. W. C. Feldman, G. F. Auchampaugh, and R. C. Byrd, "A Novel Fast Neutron Detector for Space Applications," *Nuclear Instruments and Methods* **A306**, 350–365 (1991).
10. G. F. Knoll, "General Properties of Radiation Detectors," in *Radiation Detection and Measurement, 2nd Ed.*, (Wiley, New York, 1989) Chaps. 3–4.
11. F. H. Fröhner, "Evaluation of ^{252}Cf Prompt Fission Neutron Data from 0 to 20 MeV by Watt Spectrum Fit," *Nuclear Science and Engineering* **106**, 345–352 (1990).
12. T. W. Bonner, "Measurements of Neutron Spectra from Fission," *Nuclear Physics* **23**, 116–121 (1961).
13. T. Wiedling, "Microscopic Fission-Neutron-Spectra Measurements," in *Neutron Standards and Flux Normalization,*" NTIS document CONF-701002, (August, 1971) pp. 437–451.
14. R. C. Byrd, "Directional Fast-Neutron Detectors," Los Alamos National Laboratory report LA-12379-MS (October 1992).

Los Alamos
NATIONAL LABORATORY
Los Alamos, New Mexico 87545